



Cite this: *Soft Matter*, 2020,
16, 1236

Active rotational dynamics of a self-diffusiophoretic colloidal motor†

Shang Yik Reigh, *^{abc} Mu-Jie Huang, *^d Hartmut Löwen, ^b Eric Lauga ^e and Raymond Kapral ^d

The dynamics of a spherical chemically-powered synthetic colloidal motor that operates by a self-diffusiophoretic mechanism and has a catalytic domain of arbitrary shape is studied using both continuum theory and particle-based simulations. The motor executes active rotational motion when self-generated concentration gradients and interactions between the chemical species and colloidal motor surface break spherical symmetry. Local variations of chemical reaction rates on the motor catalytic surface with catalytic domain sizes and shapes provide such broken symmetry conditions. A continuum theoretical description of the active rotational motion is given, along with the results of particle-based simulations of the active dynamics. From these results a detailed description of the factors responsible for the active rotational dynamics can be given. Since active rotational motion often plays a significant part in the nature of the collective dynamics of many-motor systems and can be used to control motor motion in targeted cargo transport, our results should find applications beyond those considered here.

Received 2nd October 2019,
Accepted 12th December 2019

DOI: 10.1039/c9sm01977d

rsc.li/soft-matter-journal

1 Introduction

Small self-propelled colloidal particles that use chemical energy derived from their environments to execute directed motion have been the subject of numerous investigations because of their potential applications and the new phenomena that arise in systems of such active colloids.^{1–7} Colloidal motors with different shapes and sizes that are propelled by various mechanisms have been made and their properties have been characterized (see *e.g.* ref. 8–12). The focus of the work described here is on the active orientational motion of motors that operate by phoretic mechanisms,^{13,14} especially through self-diffusiophoresis.^{3,5,15–17}

The self-diffusiophoretic mechanism operates for colloidal particles whose surfaces have catalytic and noncatalytic domains. Under nonequilibrium conditions, chemical reactions on the catalytic portion of the colloid surface generate fuel and product

concentration gradients that give rise to pressure gradients on the fluid and shear stresses on the particle derived from the fluid–colloid interaction potentials. Since no external forces are present, momentum conservation leads to fluid flows in the surrounding medium that are responsible for motor motion.

Most studies of diffusiophoretic motors have considered the simplest motor geometry: spherical Janus motors with catalytic and noncatalytic hemispherical caps.^{1,8,14,18,19} As a consequence of axial symmetry these motors execute active directed motion along the polar axis of the motor but their orientational dynamics is controlled solely by rotational Brownian motion. Janus motors with variable cap sizes that retain the axial symmetry of the colloid have also been studied but, like the Janus motors with hemispherical caps, they cannot execute active rotational motion.^{9,10,12,20} However, active rotational motion is obtained if the axial symmetry of the spherical colloid is broken by asymmetrical catalytic domains, for example, inhomogeneous catalytic reaction rates²¹ or asymmetrical distribution of catalytic domains on the motor surface.²² Active rotational motion has also been studied for Janus motors with a coupling of electrochemical forces to fluid flow²³ or under an external field such as gravity,²⁴ nonspherical colloidal motors including L-shaped particles^{25,26} and dimer aggregates of motors.^{27–32}

In this paper we investigate self-diffusiophoretic spherical Janus motors with catalytic domains that break the axial symmetry of the colloid and undergo active rotational motion. Experimental realizations of Janus colloids with such catalytic domains have been made by glancing angle metal evaporation.²¹ Catalytic domains made by this process have variable thickness and

^a The Research Institute of Basic Sciences, Seoul National University, Seoul 08826, Republic of Korea. E-mail: silee@snu.ac.kr

^b Institut für Theoretische Physik II: Weiche Materie, Heinrich-Heine-Universität Düsseldorf, 40225 Düsseldorf, Germany

^c Max-Planck-Institut für Intelligente Systeme, Heisenbergstraße 3, 70569 Stuttgart, Germany

^d Chemical Physics Theory Group, Department of Chemistry, University of Toronto, Toronto, Ontario M5S 3H6, Canada. E-mail: mj.huang@utoronto.ca

^e Department of Applied Mathematics and Theoretical Physics, Center for Mathematical Science, University of Cambridge, Wilberforce Road, Cambridge CB3 0WA, UK

† Electronic supplementary information (ESI) available: A video showing the active rotational motion of a Janus motor with an asymmetrical catalytic domain (Movie S1). See DOI: 10.1039/c9sm01977d

evidence suggests that propulsion occurs largely through an electrophoretic mechanism where the catalytic activity depends on the thickness of the metal coating,³³ although it has also been suggested that active rotation can arise solely due to diffusiophoresis. In the following we present the full continuum theoretical description of the self-diffusiophoretic active rotational dynamics of Janus colloids with catalytic domains of arbitrary shape, along with particle-based simulations of the translational and rotational dynamics of such Janus colloids. We show that both the domain shape and spatial variations of the catalytic activity play important roles in determining the nature and magnitude of the active rotational motion.

The outline of the paper is as follows. Section 2 gives the general expressions for the linear and angular propulsion velocities, along with the solutions of the reaction–diffusion equations for the concentration fields that enter these formulae. Simulations of the Janus motor dynamics are presented in Section 3 where the spatial structure of the concentration fields is studied in detail as a function of the catalytic domain shape and spatial dependence of the reaction rate. In addition, various aspects of the active rotational motion and its effects on the motor mean square displacement are presented. Section 4 contains the conclusions of the study, while the Appendix provides details of the simulation method.

2 Continuum theory

2.1 Linear and angular motor velocities

We consider a spherical motor with hydrodynamic radius R_M immersed in fluid with dynamic viscosity η and density ρ comprising reactive A (fuel) and B (product) particles. The motor has a catalytic (C) region with an arbitrary shape on its surface while the rest of the surface is noncatalytic (N). Assuming that catalytic reactions on the motor surface strongly favor the formation of products, we consider only the forward reactions, $C + A \xrightarrow{k_0} C + B$, to occur with an intrinsic reaction rate k_0 . In order to maintain the system in a nonequilibrium state we also suppose that a chemical reaction $B \xrightarrow{k_2} A$ occurs by a different mechanism in the fluid phase; e.g., by a reaction $E + B \xrightarrow{k_3} F + A$, where the fixed concentration of species [E] is incorporated in the rate constant $k_2 = k_3[E]$ and can be used to vary the value of k_2 . The introduction of fluid-phase reactions to supply fuel and remove product mimics the way these processes occur in biological contexts, and they can be implemented in *in vitro* experiments. They are especially important for the particle-based simulations described below since the system must be maintained in a nonequilibrium state for long time periods to extract reliable statistical data on motor motion.^{34,35}

The deterministic force and torque on a colloidal motor can be computed from surface averages of the fluid pressure tensor with boundary conditions that account for values of the fluid velocity fields on the surface and diffusiophoretic coupling to the chemical species concentration gradients.^{14,36} For partial slip boundary conditions on the surface of the colloid, they take the

following forms on time scales longer than the hydrodynamic time, $R_M^2\rho/\eta$:^{37,38}

$$\mathbf{F} = \frac{\zeta_t^\circ}{4\pi R_M^2(1+3b/R_M)} \sum_{h=C}^N \lambda_h \int_S dS H_h(\theta, \phi) [(\mathbf{I} - \hat{\mathbf{r}}\hat{\mathbf{r}}) \cdot \nabla c_B(\mathbf{r})], \quad (1)$$

$$\mathbf{T} = \frac{3\zeta_r^\circ}{8\pi R_M^3(1+3b/R_M)} \sum_{h=C}^N \lambda_h \int_S dS H_h(\theta, \phi) [\hat{\mathbf{r}} \times \nabla c_B(\mathbf{r})], \quad (2)$$

where \mathbf{I} is the unit dyadic, $\hat{\mathbf{r}}$ is the outward normal unit vector from the sphere surface, $c_B(\mathbf{r})$ is the concentration of species B at \mathbf{r} , b is the slip length, and ζ_t° and ζ_r° are the translational and rotational friction coefficients for perfect stick boundary condition ($b = 0$). Here the function $H_h(\theta, \phi) = 1$ if the angles θ and ϕ lie in a surface domain of type h , otherwise $H_h(\theta, \phi) = 0$, where $h = C$ or N , and $\lambda_h = k_B T (\lambda_h^{(1)} + b \lambda_h^{(0)}) / \eta$ with

$$\lambda_h^{(n)} = \int_0^\infty dr r^{(n)} \left[e^{-U_{hk}(r)/k_B T} - e^{-U_{hA}(r)/k_B T} \right], \quad (3)$$

where $U_{hk}(r)$ is the interaction potential between fluid particles of species $k = A, B$ and motor surface of type h . While perfect stick boundary conditions are usually considered for micrometric and larger particles, partial slip boundary conditions apply for colloids with hydrophobic interactions and have been suggested to give rise to enhancement of interfacially driven transport phenomena.³⁹ The colloidal particles considered in the simulations presented below have repulsive interactions with the fluid and satisfy partial slip boundary conditions.

The translational ζ_t and rotational ζ_r friction coefficients of the spherical colloid are³⁸

$$\zeta_t = \zeta_t^\circ \frac{1+2b/R_M}{1+3b/R_M}, \quad \zeta_r = \frac{\zeta_r^\circ}{1+3b/R_M}, \quad (4)$$

and it then follows that the diffusiophoretic translational and angular velocities are given by

$$\mathbf{V} = \mathbf{F}/\zeta_t, \quad \boldsymbol{\Omega} = \mathbf{T}/\zeta_r. \quad (5)$$

In this paper we consider motor dynamics for two situations: (1) the interactions of the A and B particles with a motor are the same for the C and N domains, and (2) these interactions differ for the two domains. For the former case we have $\lambda_C = \lambda_N = \lambda$ and the formulas for the linear and angular velocities reduce to

$$\mathbf{V} = \frac{\lambda}{4\pi R_M^2(1+2b/R_M)} \int_S dS [(\mathbf{I} - \hat{\mathbf{r}}\hat{\mathbf{r}}) \cdot \nabla c_B(\mathbf{r})], \quad (6)$$

$$\boldsymbol{\Omega} = \frac{3\lambda}{8\pi R_M^3} \int_S dS [\hat{\mathbf{r}} \times \nabla c_B(\mathbf{r})]. \quad (7)$$

For the latter case, considering only the C domain to be responsible for self propulsion, one has $\lambda_N = 0$ and the expressions for the velocities become

$$\mathbf{V} = \frac{\lambda_C}{4\pi R_M^2(1+2b/R_M)} \int_S dS H_C(\theta, \phi) [(\mathbf{I} - \hat{\mathbf{r}}\hat{\mathbf{r}}) \cdot \nabla c_B(\mathbf{r})], \quad (8)$$

$$\Omega = \frac{3\lambda_C}{8\pi R_M^3} \int_S dS H_C(\theta, \phi) [\hat{r} \times \nabla c_B(r)]. \quad (9)$$

In this case one can see from eqn (9) that active rotation takes place when the distribution of concentration gradients over the C domain must have broken symmetry in the plane of the motor rotation.

2.2 Concentration field

The concentration fields that enter the expressions for the linear and angular velocities can be obtained from the solutions of reaction-diffusion equations. For small Péclet numbers, $\text{Pe} = VR_M/D \ll 1$, where D is the diffusion coefficient of the A and B species, we solve the steady state reaction-diffusion equation for the concentration c_A of species A,

$$D\nabla^2 c_A - k_2 c_A = 0, \quad (10)$$

subject to the radiation boundary condition on the motor surface,

$$-\mathbf{J} \cdot \hat{\mathbf{r}}|_{r=R_c} = \mathcal{R} c_A(r=R_c), \quad (11)$$

where R_c is the radius at which surface chemical reactions occur and \mathbf{J} is the flux of species A given by $\mathbf{J} = -D\nabla c_A$. The concentration c_B of species B can be found from the mass conservation condition, $c_A + c_B = c_0 = \text{const}$.

In eqn (11) \mathcal{R} denotes the chemical reaction rate on the catalytic domain. It may be written as the product of the rate coefficient $k_0(\theta, \phi)$, which in general depends on angles, and the step function $H_C(\theta, \phi)$, $\mathcal{R} = k_0(\theta, \phi)H_C(\theta, \phi)/(4\pi R_c^2)$. Using this form the boundary condition in eqn (11) may be written as

$$k_D k \frac{\partial c_A}{\partial r}|_{r=R_c} = k_0(\theta, \phi) H_C(\theta, \phi) c_A(r=R_c), \quad (12)$$

where the Smoluchowski diffusion-controlled rate coefficient is given by $k_D = 4\pi R_c D$.

The reaction-diffusion eqn (10) in spherical polar coordinates, (r, θ, ϕ) , can be solved by separation of variables and the solution for c_B can be written as

$$c_B = c_0 \sum_{n=0}^{\infty} \sum_{m=-n}^n A_{nm} \frac{R_n(r)}{R_n(R_c)} Y_{nm}(\theta, \phi), \quad (13)$$

with radial part

$$R_n(r) = \sqrt{\frac{\pi}{2\kappa_2 r}} K_{n+\frac{1}{2}}(\kappa_2 r), \quad (14)$$

where $\kappa_2 = \sqrt{k_2/D}$ and $K_{n+1/2}$ is a modified Bessel function of the second kind. The angular part is given in terms of spherical harmonics,

$$Y_{nm}(\theta, \phi) = a_{nm} P_{nm}(\theta, \phi) e^{im\phi}, \quad (15)$$

where P_{nm} is an associated Legendre function, and $a_{nm} = \sqrt{(2n+1)/4\pi} \cdot \sqrt{(n-m)!/(n+m)!}$. The solution is expressed in a body-fixed frame (see Fig. 1).

The unknown coefficients A_{nm} in the concentration field are found by inserting $c_A = c_0 - c_B$ determined from eqn (13) into

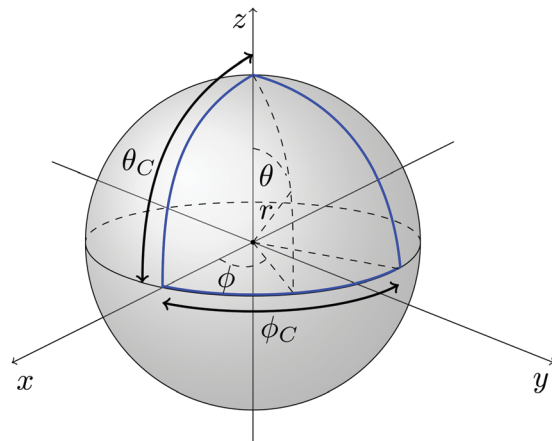


Fig. 1 A model of the motor with a catalytic domain specified in spherical polar coordinates (r, θ, ϕ) with polar angle θ_C and azimuthal angle ϕ_C with respect to the Cartesian coordinates (x, y, z) . The small region surrounded by the solid blue lines ($0 < \theta < \theta_C$ and $0 < \phi < \phi_C$) is the catalytic domain while the rest of the surface is noncatalytic.

the boundary condition (12). Use of the orthogonality of the spherical harmonics leads to the following set of equations:

$$\sum_{n=0}^{\infty} \sum_{m=-n}^n M_{n'm'nm} A_{nm} = \gamma_{n'm'}, \quad (16)$$

where

$$\begin{aligned} M_{n'm'nm} &= \alpha_{n'm'nm} + \beta_{n'm'nm}, \\ \alpha_{n'm'nm} &= \left\{ \kappa_2 R_M \frac{R_{n+1}(R_c)}{R_n(R_c)} - n \right\} \delta_{n'n} \delta_{m'm}, \\ \beta_{n'm'nm} &= \frac{1}{k_D} \int_0^{2\pi} \int_0^\pi k_0(\theta, \phi) H(\theta, \phi) Y_{nm} Y_{n'm'}^* \sin \theta d\theta d\phi, \\ \gamma_{n'm'} &= \frac{1}{k_D} \int_0^{2\pi} \int_0^\pi k_0(\theta, \phi) H(\theta, \phi) Y_{n'm'}^* \sin \theta d\theta d\phi, \end{aligned} \quad (17)$$

where δ_{nm} is the Kronecker delta. If $H_C(\theta, \phi)$ is expanded in series of spherical harmonics, one can obtain explicit expressions for the coefficients A_{nm} in terms of the coefficients in this series expansion.²²

For small κ_2 , the radial part of eqn (13) reduces to

$$R_n(r) = \frac{\pi(2n)!}{n!} \left(\frac{1}{2\kappa_2 r} \right)^{n+1}, \quad (18)$$

and in the limit of vanishing fluid phase reactions ($k_2 \rightarrow 0$), corresponding to a source for fuel particles and a sink for product particles far from the colloid, the concentration field of B particles becomes

$$c_B = c_0 \sum_{n=0}^{\infty} \sum_{m=-n}^n A_{nm} \left(\frac{R_c}{r} \right)^{n+1} Y_{nm}(\theta, \phi), \quad (19)$$

where the coefficients A_{nm} are determined by eqn (16) and (17) except that $\alpha_{n'm'nm}$ is given by

$$\alpha_{n'm'nm} = (n+1)\delta_{n'n}\delta_{m'm}. \quad (20)$$

If the catalytic domain has form of a spherical triangle, it can be specified by the angles θ_C and ϕ_C as the region where $0 \leq \theta \leq \theta_C$ and $0 \leq \phi \leq \phi_C$ (see Fig. 1). Since $H_C(\theta, \phi) = 1$ for $(0 \leq \theta \leq \theta_C, 0 \leq \phi \leq \phi_C)$ and 0 otherwise, $\beta_{n'm'nm}$ and $\gamma_{n'm'}$ in eqn (17) can be written as

$$\begin{aligned} \beta_{n'm'nm} &= \frac{1}{k_D} \int_0^{\theta_C} \int_0^{\phi_C} k_0(\theta, \phi) Y_{nm} Y_{n'm'}^* \sin \theta d\theta d\phi, \\ \gamma_{n'm'} &= \frac{1}{k_D} \int_0^{\theta_C} \int_0^{\phi_C} k_0(\theta, \phi) Y_{n'm'}^* \sin \theta d\theta d\phi. \end{aligned} \quad (21)$$

For a Janus motor with a hemispherical catalytic cap, one has $\theta_C = \pi/2$ and $\phi_C = 2\pi$. If the catalytic activity is uniform, i.e. $k_0(\theta, \phi) = \tilde{k}_0 = \text{const}$, one sees that only the $m = m' = 0$ term remains in eqn (16), (17) and (21) since $M_{n'm'nm} = 0$ for $m \neq m'$ and $\gamma_{n'm'} = 0$ for $m' \neq 0$, which gives $A_{nm} = 0$ for all n and $m \neq 0$. Hence $\alpha_{n'm'nm}$, $\beta_{n'm'nm}$, and $\gamma_{n'm'}$ for $m = m' = 0$ are given by

$$\begin{aligned} \alpha_{n'0n0} &= a_{n0} \left\{ \kappa_2 R_c \frac{R_{n+1}(R_c)}{R_n(R_c)} - n \right\} \frac{2}{2n+1} \delta_{n'n}, \\ \beta_{n'0n0} &= a_{n0} \frac{k_0}{k_D} \int_0^1 P_{n0} P_{n'0} d\mu, \quad \gamma_{n'0} = \frac{k_0}{k_D} \int_0^1 P_{n'0} d\mu, \end{aligned} \quad (22)$$

where the integrals have analytic expressions.⁴⁰ In this case one obtains the B concentration field as

$$c_B = c_0 \sum_{n=0}^{\infty} a_{n0} A_{n0} \frac{R_n(r)}{R_n(R_c)} P_n(\theta, \phi), \quad (23)$$

which is consistent with previously given solutions.^{41,42}

2.3 Linear and angular velocities for special cases

2.3.1 Uniform λ ($\lambda = \lambda_C = \lambda_N$). If the interaction potentials have no angular dependence, for instance by setting $U_{CA} = U_{NA} \neq U_{CB} = U_{NB}$ where the A and B particle interaction potentials do not depend on the domain type, one has $\lambda = \lambda_C = \lambda_N$. The self-propulsion properties and fluid flow fields of Janus motors with hemispherical caps and such interaction potentials were studied previously.⁴²

The propulsion velocities in the body-fixed frame with Cartesian coordinate unit normal vectors $\{\hat{x}, \hat{y}, \hat{z}\}$ (Fig. 1) may be obtained using eqn (8) and (13). Noting that $m = \pm 1$ is sufficient for this calculation, one finds that the x -component of the propulsion velocity, $V_x = \mathbf{V} \cdot \hat{x}$, is given by

$$\begin{aligned} V_x &= \frac{\lambda}{4R_M(1+2b/R_M)} \sum_{n=1}^{\infty} c_0 a_{n,1} (A_{n,1} - A_{n,-1}) \\ &\times \int_0^{\pi} \left(\frac{dP_{n,-1}}{d\theta} \cos \theta \sin \theta d\theta + P_{n,1} \right) d\theta. \end{aligned} \quad (24)$$

The integral in eqn (24) may be evaluated to yield $-8\delta_{n,1}/3$ giving

$$V_x = \frac{2\lambda}{3R_M(1+2b/R_M)} c_0 a_{11} (A_{1,-1} - A_{1,1}). \quad (25)$$

In a similar manner one finds

$$V_y = -\frac{2\lambda i}{3R_M(1+2b/R_M)} c_0 a_{11} (A_{1,-1} + A_{1,1}), \quad (26)$$

$$V_z = \frac{2\lambda}{3R_M(1+2b/R_M)} c_0 a_{10} A_{10}, \quad (27)$$

for the y and z components.

The angular velocity components in the body-fixed frame may be calculated from eqn (7) and one finds that they are zero since the sum of the concentration gradients around the sphere becomes zero.

2.3.2 Nonuniform λ ($\lambda_C > \lambda_N = 0$). Active motor rotation is obtained if the interaction potentials depend on type of surface domain. For example, this is the case if $\lambda_C > \lambda_N = 0$, for which the linear and angular velocities are given by eqn (8) and (9). This case encompasses situations where the A and B particles interact differently with the C and N domains ($U_{CB} \neq U_{NB}$, $U_{CA} \neq U_{NA}$). The components of the propulsion velocity are given by

$$\begin{pmatrix} V_x \\ V_y \\ V_z \end{pmatrix} = \sum_{n=0}^{\infty} \sum_{m=-n}^n \alpha_{nm} \begin{pmatrix} E_{nm} \\ F_{nm} \\ G_{nm} \end{pmatrix}, \quad (28)$$

where $\alpha_{nm} = \lambda_C c_0 a_{nm} A_{nm} / (4\pi R_M(1+2b/R_M))$ and

$$\begin{pmatrix} E_{nm} \\ F_{nm} \\ G_{nm} \end{pmatrix} = \int_0^{\theta_C} \frac{dP_{nm}}{d\theta} \sin \theta \begin{pmatrix} \cos \theta \\ \cos \theta \\ \sin \theta \end{pmatrix} d\theta \int_0^{\phi_C} \begin{pmatrix} \cos \phi \\ -\sin \phi \\ -1 \end{pmatrix} e^{im\phi} d\phi \\ - im \int_0^{\theta_C} P_{nm} d\theta \int_0^{\phi_C} \begin{pmatrix} \sin \phi \\ \cos \phi \\ 0 \end{pmatrix} e^{im\phi} d\phi. \quad (29)$$

The components of the angular velocity are

$$\begin{pmatrix} \Omega_x \\ \Omega_y \\ \Omega_z \end{pmatrix} = \sum_{n=0}^{\infty} \sum_{m=-n}^n \beta_{nm} \begin{pmatrix} H_{nm} \\ I_{nm} \\ J_{nm} \end{pmatrix}, \quad (30)$$

where $\beta_{nm} = 3\lambda_C c_0 a_{nm} A_{nm} / 8\pi R_M^2$ and

$$\begin{pmatrix} H_{nm} \\ I_{nm} \\ J_{nm} \end{pmatrix} = - \int_0^{\theta_C} \frac{dP_{nm}}{d\theta} \sin \theta d\theta \int_0^{\phi_C} \begin{pmatrix} \sin \phi \\ \cos \phi \\ 0 \end{pmatrix} e^{im\phi} d\phi \\ + im \int_0^{\theta_C} P_{nm} \begin{pmatrix} \cos \theta \\ \cos \theta \\ \sin \theta \end{pmatrix} d\theta \int_0^{\phi_C} \begin{pmatrix} -\cos \phi \\ \sin \phi \\ 1 \end{pmatrix} e^{im\phi} d\phi. \quad (31)$$

3 Simulation of motor dynamics

Particle-based simulations of motors undergoing active rotational and translational motion were carried out. The Janus motor is made from a collection of small spherical particles (beads) linked to form a large colloidal particle.^{34,35,43} The beads may be chosen to be catalytic or noncatalytic so that Janus colloids with specifically-shaped catalytic domains can be constructed. In the simulations the Janus motor is placed in a cubic box of linear size $L = 50$ with periodic boundary conditions. The fluid is composed of $N_s (= N_A + N_B)$ point particles with N_A fuel (A) and N_B product (B). The motor is made from N_b beads, residing within a sphere of radius R_j linked by stiff harmonic springs whose equilibrium lengths are chosen such that the moment of inertia tensor is nearly diagonal (see Fig. 2).³⁴ Of the total N_b beads, N_C are catalytic and N_N are noncatalytic, $N_b = N_C + N_N$. The lower hemisphere of the motor is composed solely of N beads, while the upper hemisphere has C and N beads with the size of the C domain determined by the angle ϕ_C (see Fig. 2). The fluid particles evolve by multiparticle collision dynamics^{44–47} and the coupling between fluid particles and motor beads is described by repulsive Lennard-Jones potentials, $U_{hk}(r) = 4\epsilon_{hk}[(\sigma/r)^{12} - (\sigma/r)^6 + 1/4]\Theta(r - r_c)$, where $h = C, N$, $k = A, B$, ϵ_{hk} is the interaction energy, σ is the effective size of a motor bead and $r_c = 2^{1/6}\sigma$ is the cutoff distance beyond which the potential function vanishes. Chemical reactions, $C + A \rightarrow C + B$, may occur when A particles encounter motor C beads, *i.e.* when A particles pass the cutoff distance r_c , and the reaction probability, $p(\mathbf{r}_i)$, is determined by the position of the nearest catalytic bead at \mathbf{r}_i in the body frame. The intrinsic reaction rate constant $k_0(\mathbf{r}_i) = \tilde{k}_0 p(\mathbf{r}_i)$, where \tilde{k}_0 is the intrinsic rate constant for unit reaction probability. To maintain a nonequilibrium steady state, fluid phase reactions $B \xrightarrow{k_2} A$ are carried out using reactive multiparticle collision dynamics.⁴⁸ Further details of the simulation method along with the parameter values used to obtain the results are provided in the Appendix. All quantities are reported in dimensionless units.

The simulations incorporate thermal fluctuations arising from the particulate nature of the fluid, and deterministic quantities, such as the motor linear and angular velocities discussed in the previous section, are obtained from the simulation data after averaging over an ensemble of realizations of the dynamics. The linear (\mathbf{V}) and angular ($\boldsymbol{\Omega}$) velocities in simulations are initially computed in the laboratory frame. In the body-fixed frame, the components of the translational (center of mass) velocity, (V_x, V_y, V_z) , are computed from the velocity in the laboratory frame by $V_q = \langle \mathbf{V}(t) \cdot \hat{\mathbf{q}}(t) \rangle$ with the principal axes $\hat{\mathbf{q}}(t) \in \{\hat{\mathbf{x}}(t), \hat{\mathbf{y}}(t), \hat{\mathbf{z}}(t)\}$ (Fig. 1), where brackets denote ensemble and time averages. The angular velocity in the body-fixed frame is computed in a similar way. Letting $\mathbf{r}_{bi}(t)$ and $\mathbf{v}_{bi}(t)$ be the position and velocity of the i th bead at time t and $\mathbf{R}_{cm}(t)$ be the center-of-mass position of the motor in the laboratory frame, the angular velocity in the laboratory frame is given by

$$\boldsymbol{\Omega}(t) = \sum_{i=1}^{N_b} m_b [\mathbf{r}_{bi}(t) - \mathbf{R}_{cm}(t)] \times [\mathbf{v}_{bi}(t) - \mathbf{V}(t)] / I, \quad (32)$$

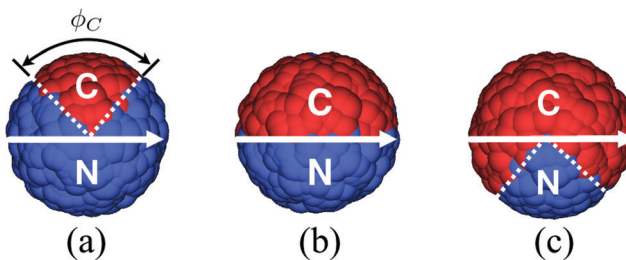


Fig. 2 Bead-spring model of motors with catalytic domains: top views from the positive z axis (*i.e.* the upper hemispheres) in Fig. 1. The catalytic domain sizes vary as shown in (a) $\phi_C = \pi/2$, (b) $\phi_C = \pi$ and (c) $\phi_C = 3\pi/2$, with a fixed $\theta_C = \pi/2$. When the chemical reaction rate on the catalytic domain depends on only the polar angle θ (for example, $k_0 = \tilde{k}_0 \cos \theta$, where \tilde{k}_0 is a constant), the motors rotate with the axes indicated by the white solid arrows due to the symmetry. The catalytic (C) and non-catalytic (N) parts are indicated by red and blue colors respectively and their approximate borderlines are shown in white dotted lines.

where $I = 2MR_j^2/5$ is the moment of inertia. Then the components of the ensemble-averaged angular velocity in the moving frame are $\Omega_q = \langle \boldsymbol{\Omega}(t) \cdot \hat{\mathbf{q}}(t) \rangle$.

Transport properties such as the translational and rotational friction coefficients can be obtained from measurements of their corresponding autocorrelation function expressions. The translational diffusion coefficient \bar{D}_t of an inactive Janus colloid (in the absence of chemical reactions), can be obtained from the time integral of the velocity correlation function,

$$\bar{D}_t = \frac{1}{3} \int_0^\infty dt \langle \mathbf{V}(t) \cdot \mathbf{V}(0) \rangle, \quad (33)$$

or, equivalently, from the mean square displacement. (Here the bar notation is used to indicate simulation values for the inactive colloid.) The translational friction coefficient $\bar{\zeta}_t$ may then be determined from the Einstein relation, $\bar{D}_t = k_B T / \bar{\zeta}_t$. The rotational diffusion coefficient \bar{D}_r can be obtained from the time integral of the orientational correlation function,

$$\frac{1}{2\bar{D}_r} = \int_0^\infty dt \langle \hat{\mathbf{u}}(t) \cdot \hat{\mathbf{u}}(0) \rangle, \quad (34)$$

where $\hat{\mathbf{u}}$ is an orientation vector, and the rotational friction coefficient $\bar{\zeta}_r$ is given by $\bar{D}_r = k_B T / \bar{\zeta}_r$.

3.1 Results for active motor translation and rotation

As discussed in Section 2.3.2, the presence of active rotational motion depends on broken symmetry rising from the forms of λ and the concentration gradients. In the following, we shall see that these two factors do indeed play important roles in active motor rotational motion.

We consider catalytic domains with shapes shown in Fig. 1 and 2. Specifically the polar angle $\theta_C = \pi/2$ is fixed but the azimuthal angle ϕ_C varies from 0 to 2π , so that the catalytic domain is confined to the upper hemisphere and its size varies with ϕ_C . Three choices, $\phi_C = \pi/2, \pi$ and $3\pi/2$, are shown in Fig. 2.

For simplicity, we suppose that the reaction rates depend only on the polar angle θ ; specifically, we take $k_0 = \tilde{k}_0 \cos \theta$, where $\tilde{k}_0 = 188.4$. The energy parameters are chosen to be $\epsilon_{NA} = \epsilon_{NB} = \epsilon_{CA} = 1 > \epsilon_{CB} = 0.1$, which gives $\lambda_C = 0.294 \neq \lambda_N = 0$ so that λ is

nonuniform. For these conditions, the catalytic domain and the concentration field are symmetric with respect to the bisectional plane $\phi = \phi_C/2$ and rotation is expected to occur about an axis perpendicular to this plane.

In addition to presenting simulation results on the active translational and rotational dynamics of the Janus motors, we will compare those results with continuum theory. The continuum theory assumes a smooth spherical particle and employs boundary conditions for the fluid velocity and concentration fields on the motor surface that account for the presence of a very thin boundary layer with length δ that is much smaller than the particle radius R_M ($\delta \ll R_M$). The Janus particle considered in the simulations is not perfectly smooth since it is constructed from beads and the boundary layer within which the fluid particles and colloid interact is of finite size with $\delta/R_M \approx 0.2$.

Since the interactions between the fluid and colloid are soft repulsive potentials, the effective hydrodynamic radius R_M may differ from the reaction distance R_c and should be determined along with the velocity slip length b . These two quantities R_M and b are estimated from eqn (4) using the simulation values of the translational (ζ_t) and rotational friction coefficients (ζ_r) for the inactive colloids and assuming $\zeta_t^\circ = 6\pi\eta R_M$ and $\zeta_r^\circ = 8\pi\eta R_M^3$. The friction coefficients may, in turn, be estimated from measured values of the corresponding diffusion coefficients. The value of $\zeta_t \sim \bar{\zeta}_t = k_B T/\bar{D}_t \simeq 500$ with $\bar{D}_t \simeq 0.002$ computed in simulations using eqn (33), and the value of the rotational friction coefficient is $\zeta_r \sim \bar{\zeta}_r = k_B T/\bar{D}_r \simeq 3620$ with $\bar{D}_r \simeq 0.000276$ obtained using eqn (34). Solving the pair of eqn (4) with the friction coefficients ζ_t and ζ_r obtained from simulations, one gets $R_M \simeq 4.61$ and $b \simeq 6.7$.

The reaction radius R_c can be determined from the simulated concentration field. For this purpose we consider a catalytic domain that occupies a quadrant of the spherical surface ($\phi_C = \pi$, $\theta_C = \pi/2$, Fig. 2(b)). Fig. 3 shows cross-sectional views in the xy and yz planes in the body-fixed frame (Fig. 1) for the product species in the motor vicinity, while quantitative comparisons are made in Fig. 4. The asymmetric concentrations (black circles) are plotted as a function of the polar angle in the bisectional symmetry plane $\phi = \phi_C/2$ (yz plane) and at the cutoff distance $r_c = 5.12$. Good agreement between simulation and continuum theory is obtained if the reaction radius is taken to be $R_c = 4.81$. This value is close to $R_M \simeq 4.61$.

Fig. 5 shows the translational and rotational motor velocities as a function of ϕ_C . As noted in Section 2.3.1, when the prefactor λ is constant ($\lambda_C = \lambda_N$), the motor has no significant active rotational motion, but only active translation, whether or not the concentration gradients are asymmetric (red and green colors). Also, there is no active rotational motion when the concentration gradients are symmetric (blue) as shown in Fig. 4, although the prefactor λ has angle dependence ($\lambda_C \neq \lambda_N$).

When the concentration gradients are asymmetric and λ depends on angles, significant active rotation is observed (black). The theory and simulations are compared for this case and the detailed simulation data are summarized in Table 1. The rotational axes lie in the xy plane so one sees that Ω_z is small

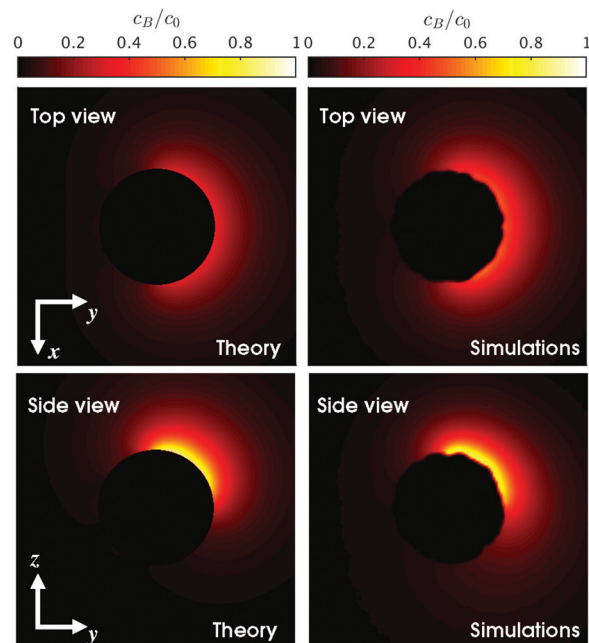


Fig. 3 Cross sectional views of the normalized chemical B (products) concentration fields (c_B/c_0) in the vicinity of the motor with a quadrant catalytic domain ($\phi_C = \pi$, $\theta_C = \pi/2$, Fig. 2(b)), where $c_A + c_B = c_0$. The left and right columns correspond to the results from theory and simulations, respectively. The first row is the top view shown in the xy plane and the second row is the side view in the yz plane (see Fig. 1).

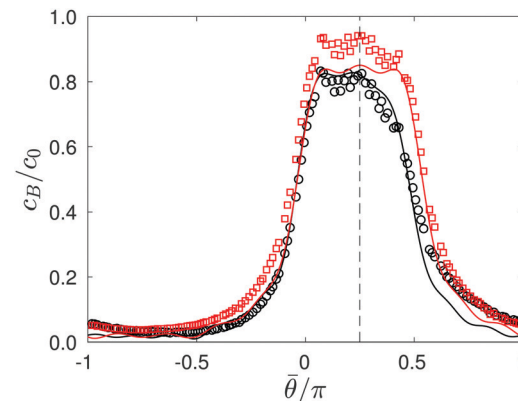


Fig. 4 Concentration distributions: quantitative comparison of theory (solid curves) and simulations (symbols) for the asymmetric (black circles, $k_0 = \tilde{k}_0 \cos \theta$) and symmetric (red squares, $k_0 = \tilde{k}_0 = \text{const}$) B concentration field with respect to the angle $\theta = \theta_C/2$ (dashed line). The motor has a quadrant catalytic domain as shown in Fig. 3. The concentration is plotted along the polar angle in the yz plane in the vicinity of the motor surface at $r = r_c = 5.12$. Here $\bar{\theta} = \theta$ when $\phi = \pi/2$ and $\bar{\theta} = -\theta$ when $\phi = 3\pi/2$. From this, R_c in continuum theory is chosen to be 4.81.

compared to the other components (see Fig. 1 and 3). Since the translational velocity depends on the reaction rate and this scales with the catalytic domain size, V increases with ϕ_C . The rotational speed Ω also increases with the domain size for the same reason when the domain size is smaller than that for a quadrant-shaped domain ($\phi_C = \pi$). However, the speed decreases if $\phi_C > \pi$ since the symmetric contributions for rotation cancel. For example when the domain with $\phi_C = 3\pi/2$ (Fig. 2(c)) is divided

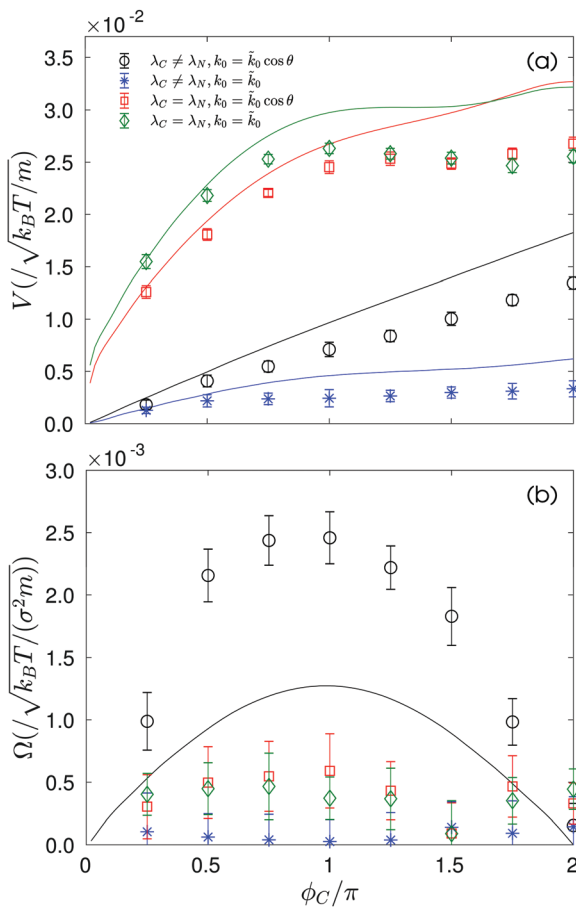


Fig. 5 (a) Translational (V) and (b) rotational motor velocity (Ω) vs. the catalytic domain size (ϕ_C). The solid lines and symbol correspond to the theory (Section 2.3) and simulations (Section 3), respectively. Black lines and circles: $\lambda_C \neq \lambda_N$, $k_0 = \tilde{k}_0 \cos \theta$. Blue lines and stars: $\lambda_C \neq \lambda_N$, $k_0 = \tilde{k}_0$. Red lines and squares: $\lambda_C = \lambda_N$, $k_0 = \tilde{k}_0 \cos \theta$. Green lines and diamonds: $\lambda_C = \lambda_N$, $k_0 = \tilde{k}_0$.

Table 1 Simulation results: ensemble-averaged translational ($\langle V_x \rangle$, $\langle V_y \rangle$, $\langle V_z \rangle$) and rotational velocity components ($\langle \Omega_x \rangle$, $\langle \Omega_y \rangle$, $\langle \Omega_z \rangle$) of the motors with various catalytic domain sizes (ϕ_C), as $\theta_C = \pi/2$ is fixed, in the body-fixed (moving) frame

ϕ_C	$\langle V_x \rangle \times 10^4$	$\langle V_y \rangle \times 10^4$	$\langle V_z \rangle \times 10^4$	$\langle \Omega_x \rangle \times 10^4$	$\langle \Omega_y \rangle \times 10^4$	$\langle \Omega_z \rangle \times 10^4$
45°	2.81	1.15	15.6	3.75	-9.14	1.12
90°	5.77	7.03	39.0	16.6	-13.7	0.51
135°	3.81	12.3	52.2	22.3	-9.86	-0.71
180°	-0.75	15.8	68.8	24.6	-0.31	-0.24
225°	-0.76	15.5	81.6	21.4	5.73	-0.96
270°	-9.17	8.39	99.3	12.4	13.5	-2.21
315°	-7.66	2.17	118	3.66	9.13	-1.45
360°	-2.08	0.25	134	1.54	-0.10	-1.10

to three parts, $0 < \phi < \pi/2$, $\pi/2 < \phi < \pi$, and $\pi < \phi < 3\pi/2$, the contributions from the first and third parts cancel and only the second part remains, which corresponds to $\phi_C = \pi/2$ (Fig. 2(a)). Hence Ω has a parabolic shape with the maximum at $\Omega = \pi$ and, as expected, the motor does not actively rotate if the entire hemisphere is covered by catalyst ($\phi_C = 2\pi$). It is interesting to note that a motor with a constant λ and k_0 does not have a

significant propulsion velocity increase for $\phi_C > \pi$, since the length of the borderline of C and N domains which has most contributions of concentration gradients does not change significantly (see Fig. 4 and ref. 42).

The continuum theory and simulations are in accord overall for different domain sizes and various parameter values but the quantitatively differences are more pronounced for the asymmetric Janus colloids compared to the previous studies for Janus motors with symmetric catalytic domains.^{42,49,50}

3.2 Colloid velocity and orientational correlations

A sample trajectory from the simulation of the dynamics of a motor with a quadrant catalytic domain ($\phi_C = \pi$) is shown in Fig. 6. One can see that the motor undergoes linear and circular motions as a result of forces and torques induced by diffusiophoretic effects. The velocity and orientational correlation functions provide quantitative information on the active dynamics of the colloid in the presence of thermal fluctuations, and we now consider these quantities. The mean square displacement of the colloid can be expressed in terms of the velocity correlation function,

$$\Delta R^2(t) = \langle (\mathbf{R}(t) - \mathbf{R}(0))^2 \rangle = \int_0^t dt_1 \int_0^t dt_2 \langle \mathbf{V}(t_1) \cdot \mathbf{V}(t_2) \rangle, \quad (35)$$

where $\mathbf{R}(t)$ is the center of mass position of the motor. The effective diffusion coefficient of the active motor can be determined from its long time behavior, $\Delta R^2(t) \sim 6D_e t$. Equivalently, the time integral of the velocity correlation function, $D_e = \frac{1}{3} \int_0^\infty dt \langle \mathbf{V}(t) \cdot \mathbf{V}(0) \rangle$, is the analog of eqn (33) for \bar{D}_t for inactive colloids. Likewise the orientational correlations for active rotation are characterized by $\langle \hat{\mathbf{u}}(t) \cdot \hat{\mathbf{u}}(0) \rangle$ considered earlier in eqn (34) for inactive colloids.

Simulations of the orientation correlation function and mean square displacement are shown in Fig. 7(a) and (b), respectively, for colloidal motors with a quadrant-shaped catalytic domain, $\phi_C = \pi$ (Fig. 3), angle dependent reaction rate, $k_0 = \tilde{k}_0 \cos \theta$, and interaction energy prefactor, $\lambda_C \neq \lambda_N$. The orientation correlation function has a decaying oscillatory structure in contrast to the exponential decay for the inactive motor, as might be anticipated for a colloid with active rotation.

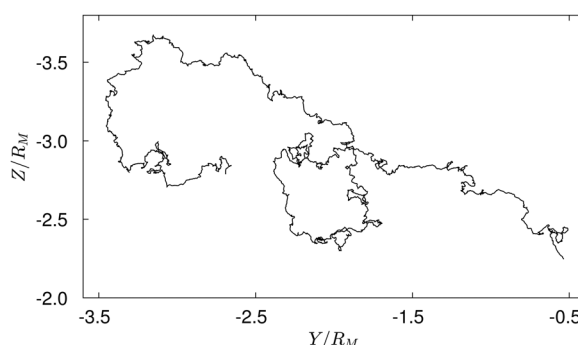


Fig. 6 A sample trajectory of the motor with a quadrant catalytic domain ($\phi_C = \pi$, Fig. 3) projected to the YZ plane in the laboratory frame is shown for a time interval $t/\tau_r \sim 2.2$. The motor rotates counter-clockwise in the YZ plane (Movie S1, ESI†).

The structures of these results can be understood in the context of overdamped Langevin models for the dynamics.⁵¹ In such models, assuming $\zeta_{t,r} \sim \bar{\zeta}_{t,r}$, the velocity of the motor $\mathbf{V}(t)$ satisfies

$$\frac{d}{dt}\mathbf{R}(t) = \mathbf{V}(t) = V\hat{\mathbf{u}}(t) + \mathbf{V}_f(t), \quad (36)$$

where the fluctuating velocity is a Gaussian white noise process with $\langle \mathbf{V}_f(t) \rangle = 0$ and fluctuation dissipation relation, $\langle \mathbf{V}_f(t_1)\mathbf{V}_f(t_2) \rangle = 2\bar{D}_r\mathbf{I}\delta(t_1 - t_2)$. The orientation of the motor $\hat{\mathbf{u}}(t)$ obeys

$$\frac{d}{dt}\hat{\mathbf{u}}(t) = (\boldsymbol{\Omega} + \boldsymbol{\Omega}_f(t)) \times \hat{\mathbf{u}}(t), \quad (37)$$

where the random angular velocity satisfies $\langle \boldsymbol{\Omega}_f(t) \rangle = 0$ and fluctuation dissipation relation, $\langle \boldsymbol{\Omega}_f(t_1)\boldsymbol{\Omega}_f(t_2) \rangle = 2\bar{D}_r\mathbf{I}\delta(t_1 - t_2)$.

For the results in Fig. 7, for simplicity in theory⁵² we assume that fluctuations apply to the orientation vector in three dimensions, i.e. $\hat{\mathbf{u}}(t) = (\cos \vartheta(t), \sin \vartheta(t) \cos \phi(t), \sin \vartheta(t) \sin \phi(t))$, and active rotational motion is restricted in a plane, for example, in the YZ plane in the laboratory frame (X, Y, Z), now parallel to the body-fixed frame, while simulations are in full three dimensions. Then the Langevin equation for the sole angle ϕ is written as

$$\frac{d}{dt}\phi(t) = \Omega + \Omega_{fx}(t), \quad (38)$$

where $\Omega_{fx}(t)$ is the X component of the random angular velocity.

Using eqn (37) and (38), the orientation correlation function neglecting the contributions from x components approximates to

$$\langle \hat{\mathbf{u}}(t) \cdot \hat{\mathbf{u}}(0) \rangle = e^{-t/\tau_r} \cos(\Omega t), \quad (39)$$

where the rotational relaxation time $\tau_r = 1/(2\bar{D}_r)$.^{27,51,53} From eqn (35), (36) and (39), the mean square displacement takes the form,

$$\Delta R^2 = 6D_e t - 2 \left(\frac{V\tau_r}{1 + (\Omega\tau_r)^2} \right)^2 \left[\left(1 - (\Omega\tau_r)^2 \right) - \left\{ \left(1 - (\Omega\tau_r)^2 \right) \cos(\Omega t) - 2\Omega\tau_r \sin(\Omega t) \right\} e^{-t/\tau_r} \right], \quad (40)$$

where the effective diffusion coefficient is given by $D_e = \bar{D}_t + V^2\tau_r/\{3(1 + (\Omega\tau_r)^2)\}$.^{27,51}

Using the diffusiophoretic linear and angular velocities in simulations, $V = 0.007$ and $\Omega = 0.00246$, respectively, the translational diffusion constant $\bar{D}_t \approx 0.002$ and the orientation relaxation time $\tau_r \approx 1810$, Fig. 7(a) compares the orientation correlation functions obtained from simulations and theory in the presence and absence of active rotation, whereas panel (b) displays the mean square displacement for the active motors. One finds good agreement.

The mean motor trajectory can be obtained from $\langle \Delta\mathbf{R}(t) \rangle = \int_0^t \langle \mathbf{V}(s) \rangle ds$. By replacing $\hat{\mathbf{u}}(t)$ by $e^{i\varphi(t)} \sin \vartheta(t)$ approximately in the complex plane (where the YZ coordinates are mapped to the complex plane and the X component is neglected) and using eqn (36), one obtains

$$\langle \mathbf{R}(t) \rangle \rightarrow \frac{V\tau_r}{\sqrt{1 + (\Omega\tau_r)^2}} e^{i(\varphi_a + \langle \varphi_0 \rangle)} \left[1 - e^{(-1/\tau_r + i\Omega)t} \right], \quad (41)$$

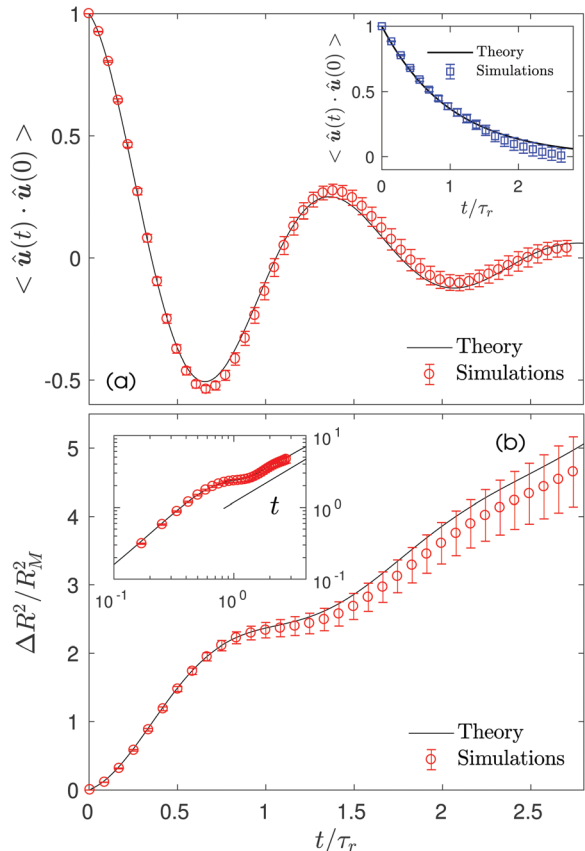


Fig. 7 (a) The orientation correlation function $\langle \hat{\mathbf{u}}(t) \cdot \hat{\mathbf{u}}(0) \rangle$ for a motor with a quadrant-shaped catalytic domain ($\phi_C = \pi$, $\lambda_C = 0.294 \neq \lambda_N = 0$) exhibiting translational and rotational motion. The inset shows the correlation function for an inactive colloid. (b) The mean square displacement $\Delta R^2(t)$ of the motor. In the inset the data are plotted in log scales and the labels are the same in the main figure. In both of these figures the black solid line and the red circles with error bars correspond to the theory and simulations, respectively, except for the inset of (a) that shows inactive motor data in blue.

where $\varphi_0 = \varphi(t=0)$ and $e^{i\varphi_a} = (1 + i\Omega\tau_r)/\sqrt{1 + (\Omega\tau_r)^2}$. In the overdamped limit, the trajectory shows a spiral pattern.⁵¹ In simulations however the motor experiences fluctuations in three dimensions and the trajectory projected on the YZ plane is shown in Fig. 6. The analytical solutions for the translational and rotational motor motion with full three dimensional fluctuations are more complex.⁵² If thermal fluctuations are not present then one sees that the motor moves in a circle with a radius V/Ω in the symmetry (YZ) plane by setting $\bar{D}_r = 1/(2\tau_r) = 0$.

4 Conclusions

This theoretical and computational investigation of the active rotational motion of self-diffusiophoretic Janus motors provided quantitative information on the nature of the asymmetrical concentration gradients and solute particle-colloid interaction potentials that give rise to this active motion. Consistent with experimental studies, the asymmetrical concentration gradients

can be produced by changing chemical reaction rates locally on the motor surface or using geometric asymmetry.^{21,27,32} Interaction energy asymmetry can arise if the fluid species interact with the catalytic and noncatalytic surface domains through different intermolecular potentials. For given interaction potentials, the domain sizes and shapes, and local variations in the reaction rates, control the motor active angular velocity. For example, in our model, the rotation radius is minimal for a quadrant domain and it increases as the domain size increases or decreases (Fig. 5).

More generally, active orientational motion plays a role in the dynamics of many-motor systems, as well as in scenarios for the control of motor motion for cargo delivery applications. The results provided in this paper should prove useful for such applications involving chemically-powered diffusiophoretic motors. The concepts discussed here for active motor rotation are not restricted to spherical shapes and diffusiophoresis but are applicable to other geometries, such as sphere-dimer motors and other phoretic mechanisms, although detailed aspects of the description will require modification.^{21,27,32,54,55}

Conflicts of interest

There are no conflicts to declare.

Appendix: simulation details

The system is composed of $N_s = N_A + N_B$ fluid A and B particles of mass m and a Janus motor comprising N_b beads of mass m and size σ linked by stiff harmonic springs.³⁴ A chemical reaction, $C + A \rightarrow C + B$, may occur when an A particle encounters a motor C bead. The reaction probability $p(\mathbf{r}_i) = \hat{\mathbf{z}} \cdot \mathbf{r}_i / |\mathbf{r}_i|$ is determined by the position of the nearest C bead at \mathbf{r}_i in the body frame, where $\hat{\mathbf{z}}$ is the z-axis in the body-fixed frame.

The interactions among fluid particles are accounted for through multiparticle collision dynamics (MPCD). This dynamics consists of streaming and collision steps at discrete time intervals h_0 with random shifts of the collision lattice to ensure Galilean invariance.^{44,45,56} The system is maintained in a steady state through irreversible reactions $B \rightarrow A$ in the fluid solution with reaction rate constant k_2 . The fluid phase reactions are carried out locally in the collision steps of MPCD.

All quantities are reported in dimensionless units. Length, energy, mass and time are measured in units of σ , $k_B T$, m , and $\sigma\sqrt{m/(k_B T)}$, respectively. The motor beads are homogeneously distributed in a sphere of radius $R_j = 4$ with the motor mass $M = mN_b = 2681$ to give neutral buoyancy of the motor. The moment of inertia $I = 2MR_j^2/5 = 24811$. The motor reaction radius used in the continuum theory is estimated by comparing the concentration field in simulations at the outer edge of the boundary layer, $r = r_c = 5.12$, which gives the reaction radius $R_c = 4.81$ (see Fig. 4). The motor is surrounded by a fluid consisting of $N_s = N_A + N_B = 1244219$ particles in the simulation box, excluding the motor volume, which gives a fluid density of $c_0 = 10$. Multiparticle collisions are carried out in each cell by performing velocity rotations by an angle $\alpha = 120^\circ$ about a

randomly chosen axis at discrete time intervals $h_0 = 0.1$. The molecular dynamics time step is $\Delta t = 0.01$. The transport properties of the fluid depend on h_0 , α , and c_0 . The fluid viscosity is given by $\eta = mc_0\nu = 7.9$, where ν is the kinematic viscosity. The common diffusion constant of A and B is $D = 0.07$. The Schmidt number is $Sc = \nu/D = 13 > 1$, which ensures that momentum transport dominates over mass transport, the Reynolds number $Re = c_0V\sigma/\eta < 0.1$ implying that viscosity is dominant over inertia, and the Péclet number $Pe = V\sigma/D < 1$ indicating diffusion dominates over fluid advection. The energy parameters for interactions between the catalytic beads and A and B species are different ($\varepsilon_{CB} = 0.1$, $\varepsilon_{CA} = 1$) while they are the same for the noncatalytic beads ($\varepsilon_{NA} = \varepsilon_{NB} = 1$). We then have, $\lambda_C = k_B T (\lambda_C^{(1)} + b\lambda_C^{(0)})/\eta \approx 0.294$ with $\lambda_C^{(0)} = 0.1$ and $\lambda_C^{(1)} = 0.476$ and $\lambda_N = 0$ since $\lambda_N^{(0)} = \lambda_C^{(1)} = 0$, and the motor moves with the catalytic domain at its head.³⁴ The intrinsic reaction rate coefficient \tilde{k}_0 is obtained from comparison of theory and simulations by setting up the rate equations with radiation boundary conditions, which gives $\tilde{k}_0 = 188.4$ through averages over multiple realizations. The reaction rate for the bulk reaction is taken to be $k_2 = 0.003$.

Acknowledgements

S. Y. Reigh greatly thanks S. Dietrich and the Max-Planck-Institute for Intelligent Systems for support. This work was supported by Brain Pool Program through the National Research Foundation of Korea (NRF) funded by the Ministry of Science and ICT (grant number: NRF-2019H1D3A2A02102052) and supported in part by the Natural Sciences and Engineering Research Council of Canada and Compute Canada. This project has also received funding from the European Research Council (ERC) under the European Union's Horizon 2020 research and innovation programme (grant agreement 682754 to EL) and from the DFG within SPP 1726. Open Access funding provided by the Max Planck Society.

References

- 1 J. Wang, *Nanomachines: Fundamentals and Applications*, Wiley-VCH, Weinheim, Germany, 2013.
- 2 W. Wang, W. Duan, S. Ahmed, T. E. Mallouk and A. Sen, *Nano Today*, 2013, **8**, 531–554.
- 3 R. Kapral, *J. Chem. Phys.*, 2013, **138**, 020901.
- 4 S. Sánchez, L. Soler and J. Katuri, *Angew. Chem., Int. Ed.*, 2014, **53**, 2–33.
- 5 A. Zöttl and H. Stark, *J. Phys.: Condens. Matter*, 2016, **28**, 253001.
- 6 C. Bechinger, R. Di Leonardo, H. Löwen, C. Reichhardt, G. Volpe and G. Volpe, *Rev. Mod. Phys.*, 2016, **88**, 045006.
- 7 R. Seemann, J.-B. Fleury and C. C. Maass, *Eur. Phys. J.: Spec. Top.*, 2016, **225**, 2227.
- 8 W. F. Paxton, K. C. Kistler, C. C. Olmeda, A. Sen, S. K. S. Angelo, Y. Cao, T. E. Mallouk, P. E. Lammert and V. H. Crespi, *J. Am. Chem. Soc.*, 2004, **126**, 13424.
- 9 M. N. Popescu, S. Dietrich, M. Tasinkevych and J. Ralston, *Eur. Phys. J. E: Soft Matter Biol. Phys.*, 2010, **31**, 351.

- 10 J. de Graaf, G. Rempfer and C. Holm, *IEEE Trans Nanobioscience*, 2015, **14**, 272.
- 11 X. Ma, A. C. Hortalao, T. Patino and S. Sanchez, *ACS Nano*, 2016, **10**, 9111.
- 12 S. Michelin and E. Lauga, *Sci. Rep.*, 2017, **7**, 42264.
- 13 B. V. Derjaguin, G. P. Sidorenkov, E. A. Zubashchenkov and E. V. Kiseleva, *Kolloidn. Zh.*, 1947, **9**, 335–347.
- 14 J. L. Anderson, *Annu. Rev. Fluid Mech.*, 1989, **21**, 61–99.
- 15 R. Golestanian, T. B. Liverpool and A. Ajdari, *Phys. Rev. Lett.*, 2005, **94**, 220801.
- 16 P. H. Colberg, S. Y. Reigh, B. Robertson and R. Kapral, *Acc. Chem. Res.*, 2014, **47**, 3504.
- 17 T. Yu, P. Chuphal, S. Thakur, S. Y. Reigh, D. P. Singh and P. Fischer, *Chem. Commun.*, 2018, **54**, 11933.
- 18 W. Wang, W. Duan, S. Ahmed, T. E. Mallouk and A. Sen, *Nano Today*, 2013, **8**, 531–554.
- 19 P. M. Wheat, N. A. Marine, J. L. Moran and J. D. Posner, *Langmuir*, 2010, **26**, 13052.
- 20 R. Golestanian, T. B. Liverpool and A. Ajdari, *New J. Phys.*, 2007, **9**, 126.
- 21 R. J. Archer, A. I. Campbell and S. J. Ebbens, *Soft Matter*, 2015, **11**, 6872–6880.
- 22 M. Lisicki, S. Y. Reigh and E. Lauga, *Soft Matter*, 2018, **14**, 3304.
- 23 J. Burelbach and H. Stark, *Phys. Rev. E*, 2019, **100**, 042612.
- 24 A. I. Campbell, R. Wittkowski, B. ten Hagen, H. Löwen and S. J. Ebbens, *J. Chem. Phys.*, 2017, **147**, 084905.
- 25 F. Kümmel, B. ten Hagen, R. Wittkowski, I. Buttinoni, R. Eichhorn, G. Volpe, H. Löwen and C. Bechinger, *Phys. Rev. Lett.*, 2013, **110**, 198302.
- 26 P. de Buyl, *Phys. Rev. E*, 2019, **100**, 022603.
- 27 S. J. Ebbens, R. A. L. Jones, A. J. Ryan, R. Golestanian and J. R. Howse, *Phys. Rev. E: Stat., Nonlinear, Soft Matter Phys.*, 2010, **82**, 015304(R).
- 28 H.-R. Jiang, N. Yoshinaga and M. Sano, *Phys. Rev. Lett.*, 2010, **105**, 268302.
- 29 S. Thakur and R. Kapral, *J. Chem. Phys.*, 2010, **133**, 204505.
- 30 A. Wittmeier, A. L. Holterhoff, J. Johnson and J. G. Gibbs, *Langmuir*, 2015, **31**, 10402.
- 31 A. Majee, *Eur. Phys. J. E: Soft Matter Biol. Phys.*, 2017, **40**, 30.
- 32 J. N. Johnson, A. Nourhani, R. Peralta, C. McDonald, B. Thiesing, C. J. Mann, P. E. Lammert and J. G. Gibbs, *Phys. Rev. E*, 2017, **95**, 042609.
- 33 S. J. Ebbens, D. A. Gregory, G. Dunderdale, J. R. Howse, Y. Ibrahim, T. B. Liverpool and R. Golestanian, *EPL*, 2014, **106**, 58003.
- 34 M.-J. Huang, J. Schofield, P. Gaspard and R. Kapral, *J. Chem. Phys.*, 2018, **149**, 024904.
- 35 M.-J. Huang, J. Schofield, P. Gaspard and R. Kapral, *J. Chem. Phys.*, 2019, **150**, 124110.
- 36 J. L. Anderson, *Ann. N. Y. Acad. Sci.*, 1986, **469**, 166–177.
- 37 P. Gaspard and R. Kapral, *J. Chem. Phys.*, 2018, **148**, 134104.
- 38 P. Gaspard and R. Kapral, *Adv. Phys.: X*, 2019, **4**, 1602480.
- 39 A. Ajdari and L. Bocquet, *Phys. Rev. Lett.*, 2006, **96**, 186102.
- 40 I. Gradshteyn and I. Ryzhik, *Table of integrals, Series, and Products*, Academic Press, New York, 7th edn, 2007.
- 41 M.-J. Huang, J. Schofield and R. Kapral, *Soft Matter*, 2016, **12**, 5581.
- 42 S. Y. Reigh, M.-J. Huang, J. Schofield and R. Kapral, *Philos. Trans. R. Soc., A*, 2016, **374**, 20160140.
- 43 P. de Buyl and R. Kapral, *Nanoscale*, 2013, **5**, 1337–1344.
- 44 A. Malevanets and R. Kapral, *J. Chem. Phys.*, 1999, **110**, 8605.
- 45 A. Malevanets and R. Kapral, *J. Chem. Phys.*, 2000, **112**, 7260.
- 46 R. Kapral, *Adv. Chem. Phys.*, 2008, **140**, 89.
- 47 G. Gompper, T. Ihle, D. M. Kroll and R. G. Winkler, *Adv. Polym. Sci.*, 2009, **221**, 1–87.
- 48 K. Rohlf, S. Fraser and R. Kapral, *Comput. Phys. Commun.*, 2008, **179**, 132.
- 49 S. Y. Reigh and R. Kapral, *Soft Matter*, 2015, **11**, 3149–3158.
- 50 S. Y. Reigh, P. Chuphal, S. Thakur and R. Kapral, *Soft Matter*, 2018, **14**, 6043.
- 51 S. van Teeffelen and H. Löwen, *Phys. Rev. E: Stat., Nonlinear, Soft Matter Phys.*, 2008, **78**, 020101(R).
- 52 R. Wittkowski and H. Löwen, *Phys. Rev. E: Stat., Nonlinear, Soft Matter Phys.*, 2012, **85**, 021406.
- 53 R. Zwanzig, *Nonequilibrium Statistical Mechanics*, Oxford University Press, New York, 2001.
- 54 M. Yang, A. Wysocki and M. Ripoll, *Soft Matter*, 2014, **10**, 6208.
- 55 B. Robertson, H. Stark and R. Kapral, *Chaos*, 2018, **28**, 045109.
- 56 T. Ihle and D. M. Kroll, *Phys. Rev. E: Stat., Nonlinear, Soft Matter Phys.*, 2001, **63**, 020201(R).